Exciting traffic jams: Nonlinear phenomena behind traffic jam formation on highways

Gábor Orosz,[1,*] R. Eddie Wilson,[2,†] Róbert Szalai,[2,‡] and Gábor Stépán[3,§]
[1]*Department of Mechanical Engineering, University of California, Santa Barbara, California 93106, USA*
[2]*Department of Engineering Mathematics, University of Bristol, Bristol BS8 1TR, United Kingdom*
[3]*Department of Applied Mechanics, Budapest University of Technology and Economics, Budapest H-1521, Hungary*
(Received 26 May 2009; published 6 October 2009)

A nonlinear car-following model is studied with driver reaction time delay by using state-of-the-art numerical continuations techniques. These allow us to unveil the detailed microscopic dynamics as well as to extract macroscopic properties of traffic flow. Parameter domains are determined where the uniform flow equilibrium is stable but sufficiently large excitations may trigger traffic jams. This behavior becomes more robust as the reaction time delay is increased.

DOI: 10.1103/PhysRevE.80.046205 PACS number(s): 05.45.−a, 45.70.Vn, 47.54.−r, 89.40.Bb

I. INTRODUCTION

Vehicular traffic has been modeled for more than half a century [1] but the precise mechanism for generation and propagation of traffic jams is still not fully understood. Recently developed numerical techniques of dynamical systems can help to shed light on the microscopic dynamics underlying the emergent behavior in these complex systems. These methods also allow one to extract macroscopic flow properties that can lead to better understanding of the fundamental principles of traffic jam formation.

It is well known that for sparse traffic there exists a uniform flow equilibrium where vehicles follow each other with the same velocity, while oscillations may arise when the traffic becomes more dense. One of the typical oscillations is a stop-and-go wave; the velocity breaks down and vehicles become densely packed on a section of the highway and the congestion propagates upstream as a density wave with a characteristic wave speed of 15–20 km/h. The congested regime of finite length is enclosed by two fronts that travel with the same velocity: a "stop-front" where vehicles enter the congested regime and a "go-front" where they leave the traffic jam. A driver may encounter such a traffic jam many minutes after it formed and many kilometers behind the place where it emerged. The name "phantom jam" is also used for these congestion waves since drivers cannot see any cause of the jam when leaving the congested regime.

There exist many different models that are able to reproduce uniform flow as well as stop-and-go waves. However, the transition between these two qualitatively different solutions is still not clarified. Here, we briefly review the basic deterministic approaches of traffic modeling and their proposed mechanisms for jam formation. Continuum or macroscopic models that characterize traffic in terms of density and velocity fields use partial differential equations (PDEs) to describe the time evolution of the system. The current state-of-the-art macroscopic models use hyperbolic PDEs [2,3]. In this setup both the uniform flow and the stop-and-go solutions are marginally stable (if they exist). Consequently, one may drive the system from one solution to the other by applying large perturbations. More precisely, a vehicle needs to come to a halt in order to lead the system to the stop-and-go state: "actions have to be as large as the effects."

Car-following or microscopic models describe vehicles as individual entities. In the simplest case the time evolution of the system is described by ordinary differential equations (ODEs) [4,5]. These models suggest that traffic jams form spontaneously when traffic becomes dense enough. More precisely, there exists a critical traffic density, below which the uniform flow is asymptotically stable but it becomes unstable above. Then even tiny fluctuations may develop into stop-and-go waves as they cascade back along the highway, i.e., "tiny actions have large effects." Clearly the hyperbolic PDE and the ODE models suggest two very different mechanisms for jam formation.

When driver reaction times are incorporated in a car-following model, delay differential equations (DDEs) describe the time evolution of the system [6–8]. In this paper, we study a simple model with reaction time delay and show that it may reconcile the conflict between the results of the PDE and ODE models by introducing an extended regime where the uniform flow is asymptotically stable but excitable, so stop-and-go jams may still emerge. Previously, excitable behavior was detected only in narrow parameter regimes and papers either focused on the mathematical analysis of the underlying bifurcations for relatively small numbers of vehicles [9,10] or conjectured excitability from numerical simulations [11,12]. Calculating the bifurcation structure explicitly for realistic numbers of vehicles and connecting the results to macroscopic traffic phenomena are current interests in the traffic community [13,14]. We remark that one may use nonhyperbolic PDEs to model the dynamics of traffic [15] and also incorporate reaction times into continuum models [16]. The effects of time delays are also shown to be significant in many other networked systems including neural networks [17,18] and gene regulatory networks [19].

The most widely used method to investigate the nonlinear dynamics of traffic is numerical simulation. Recently, meth-

*gabor@engineering.ucsb.edu
†re.wilson@bristol.ac.uk
‡r.szalai@bristol.ac.uk
§Also at Research Group on Dynamics of Vehicles and Machines, Hungarian Academy of Sciences, Budapest H-1521, Hungary; stepan@mm.bme.hu

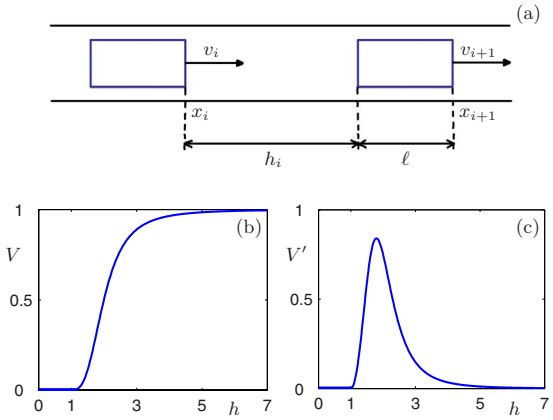

FIG. 1. (Color online) A sketch of two vehicles following each other is displayed in panel (a) while the optimal velocity function Eq. (6) and its first derivative are shown in panels (b) and (c), respectively.

ods from dynamical systems theory (normal form calculations and numerical continuation) have also been applied to investigate traffic dynamics [9,20–23]. The advantage of these methods is that both stable and unstable solutions can be studied. Indeed, unstable motions can hardly be observed in the physical system but they can influence the emergent behavior by "separating" qualitatively different stable motions. In this paper, we apply numerical continuation techniques [24] to reveal the intricate microscopic dynamics underlying jam formation and to extract macroscopic flow properties.

The layout of the paper is the following: We introduce the car-following model in Sec. II and review the bifurcation analysis of the uniform flow in Sec. III. Numerical continuation techniques are introduced in Sec. IV. They are applied to the traffic model in Sec. V where the fundamental dynamical principles behind excitability are explained. The limit of infinitely many vehicles is discussed in Sec. V A and the spatial motion of waves is studied in Sec. V B. The full nonlinear dynamics is presented in Sec. VI and we conclude our research and discuss future directions in Sec. VII.

II. CAR-FOLLOWING MODELS WITH REACTION TIME DELAY

Here, we discuss general modeling issues and introduce the specific model analyzed in this paper. Assuming identical vehicles and nearest neighbor interactions, the acceleration of the i-th vehicle is given by

$$\dot{v}_i(t) = f(h_i(t-\tau_1), \dot{h}_i(t-\tau_2), v_i(t-\tau_3)), \tag{1}$$

where the dot stands for differentiation with respect to time t, v_i is the velocity of the i-th vehicle while h_i is the bumper-to-bumper distance between the i-th and the $i+1$-st vehicles also called the headway; see Fig. 1(a). The reaction time delays τ_1, τ_2, $\tau_3 \geq 0$ are generally different, but sometimes, for the sake of simplicity, they are considered to be equal to each other or to be zero. In this paper, we focus on the effects of τ_1. Figure 1(a) shows that the headway can be defined as

$$h_i(t) = x_{i+1}(t) - x_i(t) - \ell, \tag{2}$$

where x_i is the position of the front bumper of the i-th vehicle and ℓ is the vehicles' length. Taking the time derivative one obtains the velocity difference

$$\dot{h}_i(t) = v_{i+1}(t) - v_i(t), \tag{3}$$

and this kinematic condition completes system Eq. (1).

One also has to specify boundary conditions. For simplicity we assume periodic boundary conditions: N vehicles are placed on a circular road of length $L+N\ell$ that yields the algebraic equation

$$\sum_{i=1}^{N} h_i(t) = L, \tag{4}$$

where L is called the effective ring length. Using this equation one may express one headway (for example, h_N) as a functions of the others and so reduce the number of dynamical variables by one. That is, system [Eqs. (1), (3), and (4)] can be written as a system of $2N-1$ DDEs. Notice that the vehicle length ℓ does not appear in the dynamical equations. The role of this parameter will be clarified in Sec. V B. Note that one may also study the system on semi-infinite roads where similar patterns can develop as on the ring road for large L and N, but convective instabilities may also need to be handled [25].

In previous studies, the case of arbitrarily many vehicles with weak nonlinearities was studied by performing normal form calculations [23] and the case of few vehicles with strong nonlinearities was investigated by numerical continuation [21,22]. Here, we analyze the case of large number of vehicles with strong nonlinearities. The results are presented for $N=33$, which is low enough to represent the detailed microscopic dynamics but high enough to compare the results to the case $N \to \infty$. Note that N is increased such that L/N is kept constant. We remark that when reproducing the results for larger number of vehicles (e.g., $N=99$), no significant deviations are found but the illustrations become more elaborate and so less instructive.

To determine the function f in Eq. (1) one needs to take into account some general modeling principles; see [13] for details. In this paper we consider a simple, yet widely accepted model, the so called optimal velocity (OV) model [4,6,9,21] where

$$f(h,\dot{h},v) = \frac{1}{T}[V(h) - v]. \tag{5}$$

In spite of its simplicity, (e.g., it does not depend on the velocity difference $\dot{h}$) this model is able to reproduce uniform flow as well as stop-and-go waves.

The parameter T is called the relaxation time (and $1/T$ is called the sensitivity). Note that T differs from the reaction times τ_1, τ_2, τ_3: the finite relaxation time represent the fact that vehicles have inertia while the reaction times are explicit time delays in the system. In this paper, we consider $\tau_1 > 0$ and $\tau_3 = 0$ to model the human behavior that drivers react to

their headway with finite reaction time τ_1 and know their current velocity instantly. (Note that τ_2 does not appear in the equations since there is no $\dot{h}$ term.)

The function V is called the OV function that satisfies the following properties:

(i) it is continuous, non-negative, and monotone increasing;

(ii) it approaches the maximum velocity v^0 for large headway, i.e., $V(h)\to v^0$ as $h\to\infty$, where the desired speed v^0 corresponds to the speed limit;

(iii) it is zero for small headway, i.e., $V(h)\equiv 0$ if $h\in[0,h_{\text{stop}}]$, where h_{stop} is called the stopping distance.

We remark that the results presented here are robust against changes in the OV function as long as it satisfies (i–iii).

Before specifying the OV function we rescale distances by h_{stop} and rescale time by h_{stop}/v^0. Consequently, velocities (including the OV function) are scaled by v^0. In this paper we use the rescaled OV function

$$V(h)=\begin{cases}0, & \text{if } h\in[0,1],\\ \dfrac{(h-1)^3}{1+(h-1)^3}, & \text{if } h\in[1,\infty),\end{cases} \tag{6}$$

that is shown together with its first derivative in Figs. 1(b) and 1(c). Notice that the rescaled speed limit is 1. By defining the dimensionless parameters

$$\alpha=\frac{h_{\text{stop}}}{Tv^0},\quad \tau=\frac{\tau_1 v^0}{h_{\text{stop}}}, \tag{7}$$

the rescaled model can be written into the form

$$\dot{v}_i(t)=\alpha[V(h_i(t-\tau))-v_i(t)], \tag{8}$$

that is closed by the rescaled versions of Eqs. (3) and (4). For approximate realistic values of parameters T, τ_1, v^0, h_{stop} see [21,23].

III. BIFURCATIONS OF THE UNIFORM FLOW

The system [Eqs. (3), (4), and (8)] possesses a uniform flow equilibrium

$$h_i(t)\equiv h^*=L/N,\quad v_i(t)\equiv v^*=V(h^*), \tag{9}$$

for $i=1,\ldots,N$ that may lose stability when the parameter h^* is varied.

To describe what kind of patterns can appear in system [Eqs. (3), (4), and (8)] we briefly summarize the results of the linear stability analysis shown in [21–23]. Linearizing the system about the uniform flow equilibrium Eq. (9), using trial solutions proportional to $e^{\lambda t}$, $\lambda\in\mathbb{C}$ and considering the critical eigenvalues $\lambda(h^*_{\text{cr}})=\pm i\omega$, one can obtain the stability curves

$$V'(h^*_{\text{cr}})=\frac{\omega}{2\cos\left(\omega\tau-\dfrac{k\pi}{N}\right)\sin\left(\dfrac{k\pi}{N}\right)},$$

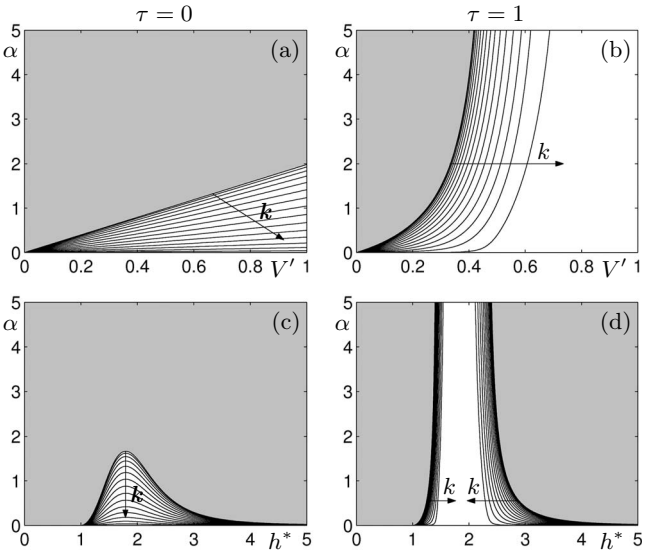

FIG. 2. Linear stability diagrams without and with reaction time delay. Domains where the uniform flow is linearly stable are shaded. Panels (a,b) show stability charts on the $(V'(h^*),\alpha)$-plane that are transformed to the (h^*,α)-plane in panels (c,d). The arrows represent the increase of wave number k.

$$\alpha=-\omega\cot\left(\omega\tau-\frac{k\pi}{N}\right), \tag{10}$$

that are parameterized by the frequency $\omega\in\mathbb{R}^+$. Here, $k\in\mathbb{Z}^+$ is a discrete wave number such that $1\le k\le N/2$. When crossing a stability curve, a Hopf bifurcation takes place, i.e., a pair of complex conjugate eigenvalues crosses the imaginary axis. The appearing small-amplitude oscillations are travelling waves with frequency ω and wave number k.

In Figs. 2(a) and 2(b) the stability curves are compared for $\tau=0$ and $\tau>0$. Notice that for $\tau=0$ the curves become the straight lines

$$\alpha=2\cos^2\left(\frac{k\pi}{N}\right)V'(h^*_{\text{cr}}), \tag{11}$$

and $\alpha\to\infty$ as $\omega\to\infty$. For $\tau>0$ the curves approach vertical asymptotes located at

$$V'(h^*_{\text{cr}})=\frac{\dfrac{k\pi}{N}}{2\tau\sin\left(\dfrac{k\pi}{N}\right)}, \tag{12}$$

when $\omega\to\frac{1}{\tau}\frac{k\pi}{N}$. That is for large enough α the curves are contained by the regime $V'\in[\frac{1}{2\tau},\frac{\pi}{4\tau}]$.

The stability curves are ordered such that the mode with lowest wave number $k=1$ (i.e., with the longest wavelength) gives the stability boundary and the curves with $k>1$ lead to further instabilities as k is increased. This means that the uniform flow loses its stability to travelling waves with long wavelength first and then waves with shorter and shorter wavelength may show up, too. This behavior is illustrated in Figs. 2(a) and 2(b) where the uniform flow is linearly stable

in the shaded domains and the arrows show the increase of wave number k. The ordering of stability curves is preserved for any feasible model Eq. (1) with zero delays $\tau_1=\tau_2=\tau_3=0$; see [13]. In the case of the delayed model Eq. (8) we found that the order is also kept for $\tau>0$.

Using the derivative of the OV function Eq. (6) in Fig. 1(c), one may transform the stability charts from the $(V'(h^*),\alpha)$-plane [Figs. 2(a) and 2(b)] to the (h^*,α)-plane [Figs. 2(c) and 2(d)]. For $\tau=0$ there is a single curve for each wave number k in the (h^*,α)-plane such that the wave number increases from outside to inside. For sufficiently large values of α the uniform flow is stable for any value of the average density h^*. For $\tau=1$ there are two curves for each wave number k with vertical asymptotes, i.e., for any values of α the uniform flow is stable for large h^* (sparse traffic) and small h^* (dense traffic) and it is unstable for intermediate values of h^*. One may check that this behavior persists as N is increased and the $N=33$ case is a good representation of the large N case. Note that in the stable regime for small h^* vehicles travel with the low velocity or stand on the freeway when $h^*\leq 1$.

We remark that for $0<\tau<3\cdot 2^{-7/3}$ the stability chart is similar to the $\tau=0$ case (but the maxima of the curves are larger). At $\tau=3\cdot 2^{-7/3}\approx 0.595$ the curve for wave number $k=1$ becomes unbounded above. When increasing τ further, curves for higher and higher wave numbers become unbounded above finishing with the curve for $k=N/2$ at $\tau=3\pi\cdot 2^{-10/3}\approx 0.935$. This can be seen by calculating the maximum of $V'(h)$ from Eq. (6) and using Eq. (12).

In the literature, stability diagrams are often plotted using the dimensional parameter $1/T$ instead of α. Then in the nondelayed case the maxima of the closed stability curves are proportional to v^0 but to obtain stability curves that are unbounded above the limit $v^0\to\infty$ needs to be taken. In the delayed case, the curves are unbounded above even for moderate values of v^0.

When h^* is close to h^*_{cr}, the small-amplitude travelling wave solution can be written into the form

$$v_i(t)=v^*+\frac{1}{2}v_{\mathrm{amp}}\cos\left(\frac{2\pi k}{N}i+\omega t\right), \tag{13}$$

for $i=1,\ldots,N$. From Eq. (10), one can determine a dispersion relation (ω as the function of k) and calculate the spatial wave speed

$$c_0=v^*-h^*V'(h^*_{\mathrm{cr}})\left[1-\mathcal{O}\left(\frac{k\pi}{N}\right)^2\right]. \tag{14}$$

At leading order the delay only influences the wave speed by changing the quantity $V'(h^*_{\mathrm{cr}})$.

To determine the peak-to-peak amplitude of oscillations v_{amp} in Eq. (13) nonlinearities has to be considered. Using third-order approximation of nonlinearities and carrying out Hopf normal form calculations, one may obtain the amplitude

$$v_{\mathrm{amp}}=2\sqrt{-\frac{\mathrm{Re}[\lambda'(h^*_{\mathrm{cr}})]}{\delta}(h^*-h^*_{\mathrm{cr}})}, \tag{15}$$

where $\lambda'(h^*_{\mathrm{cr}})$ describes the "speed" of crossing the imaginary axis by the critical eigenvalue $\lambda(h^*_{\mathrm{cr}})=\mathrm{i}\omega$ as the parameter h^* is varied. For $\delta<0$ the Hopf bifurcations are supercritical (small amplitude oscillations appear after the pair of complex conjugate eigenvalues crosses the imaginary axis), while for $\delta>0$ they are subcritical (oscillations appear before the eigenvalues cross the imaginary axis). For $k=1$ supercriticality results in stable small-amplitude waves while subcriticality gives unstable ones. For $k>1$ both cases lead to unstable waves as will be discussed in Secs. V and VI. It was shown in [23] that when the delay is included in the model, the bifurcations are robustly subcritical and δ was given in a closed form for arbitrary N.

Indeed, the wave speed Eq. (14) and the amplitude Eq. (15) are only good approximations for small-amplitude oscillations when h^* is close to h^*_{cr}. To describe the behavior far from the bifurcation points one needs to use numerical methods.

IV. NUMERICAL CONTINUATION TECHNIQUES

In this section, we provide the reader with some details about the numerical continuation techniques that are the principal tools of investigation in the subsequent sections. Those who are familiar with such techniques may skip this section. The main advantage of these methods, compared to numerical simulation, is that both stable and unstable states can be studied. For ODEs one can use the package AUTO [26] while for DDEs the packages DDE-BIFTOOL [27] and PDDE-CONT [28] are available. We describe the capabilities of these packages that are exploited in this paper; for more details see [24].

Numerical continuation packages are able to follow branches of equilibria and periodic solutions as a parameter is varied. Stability information is computed along the branches and bifurcation points—where the stability of solutions changes—are detected automatically. For example, considering the DDE [Eqs. (3), (4), and (8)] one may fix τ and α, vary the parameter h^* and study the uniform flow equilibrium and the oscillations arising at the Hopf bifurcation points.

Substituting the uniform flow equilibrium into the DDE results in algebraic equations. For a chosen parameter h^*, these can be solved numerically by using an initial guess and the Newton-Raphson method. Then the result can be used as an initial approximation when solving the same set of algebraic equations for the slightly changed parameter $h^*+\mathrm{d}h^*$. By continuing this process, a branch of equilibria is obtained as a function of the bifurcation parameter. Indeed, this is a numerical representation of Eq. (9).

To determine the stability of equilibria the linearization of the DDE is considered and the corresponding complex eigenvalues $\lambda\in\mathbb{C}$ are computed numerically. There are infinitely many eigenvalues but only finitely many are located on the right side of a chosen vertical boundary in the complex plane. The uniform flow equilibrium is stable when all

eigenvalues are located on the left-half complex plane. Hopf bifurcations of equilibria are detected when a pair of complex conjugate eigenvalues crosses the imaginary axis at $\pm i\omega$.

To be able to follow the branches of arising periodic solutions the oscillations are represented on a finite mesh with a (small) number of so-called collocation points in between the mesh points. On each mesh interval the solution is given by a polynomial and the degree of the polynomial is equal to the number of collocation points. In the close vicinity of the Hopf bifurcation points the first harmonics with frequency ω [cf. Eq. (13)] can be used as initial approximation for the periodic orbits and these can be corrected by the Newton-Raphson method. Then, similarly to equilibria, branches of periodic orbits can be continued by using the solution at a certain branch point as an initial approximation for the next branch point.

To determine the stability of oscillatory solutions the solution operator of the DDE is discretized and the eigenvalues of the resulting large matrix, the Floquet multipliers, are calculated. There are infinitely many Floquet multipliers but only finitely many are located outside a chosen neighborhood of the origin. The periodic solutions are stable when all Floquet multipliers are located inside the unit circle (except a trivial multiplier at +1 corresponding to continuous translational symmetry along the periodic orbit). Fold bifurcations of periodic solutions are detected when an additional real Floquet multiplier crosses the unit circle at +1. Since the branch folds back in this case, arclength parametrization of the curve is implemented.

It is also possible to fix only the parameter τ and vary the remaining two parameters h^* and α while prescribing the additional constraint that a bifurcation occurs. For example, considering the uniform flow equilibrium and assuming that Hopf bifurcation occurs (i.e., there exists a pair of purely imaginary eigenvalues $\pm i\omega$), the Hopf bifurcation curves in the (h^*, α)-plane can be traced numerically. More importantly, considering periodic solution and assuming that fold bifurcation occurs (i.e., there exist a double Floquet multiplier at +1), fold bifurcation curves can be traced in the (h^*, α) parameter plane. We remark that for DDEs this can only be achieved by using the recently developed package PDDE-CONT [28].

We emphasize that the application of continuation packages is a much more efficient way of exploring parameter space than performing mass ensemble simulation of the initial value problem. This is especially true for DDEs where the initial conditions are functions in the interval $t \in [-\tau, 0]$.

V. NONLINEAR DYNAMICS BEHIND EXCITABILITY

In Sec. III, we determined that the stability curve for $k=1$ gives the stability boundary. In this section we focus on the nonlinear behavior arising from this long wavelength instability by using the techniques described in Sec. IV. These methods allow us to reveal the intricate microscopic dynamics of the system including hidden unstable oscillations. Moreover, macroscopic properties of the flow can also be extracted.

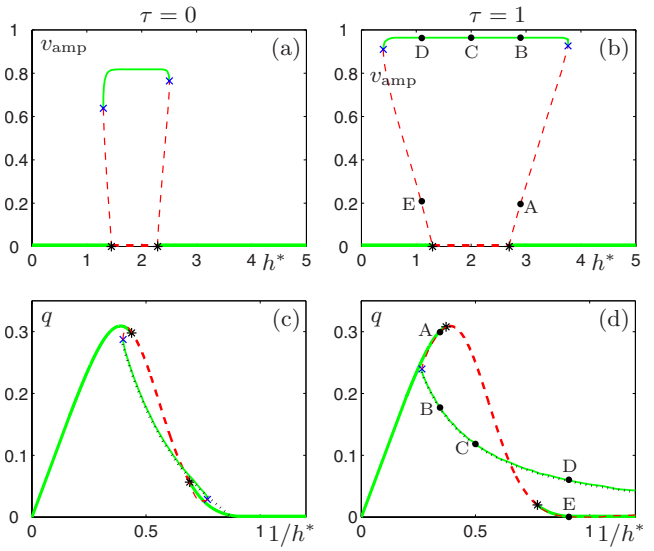

FIG. 3. (Color online) Bifurcation diagrams for the lowest wave number $k=1$ without and with reaction time delay in case of $\alpha=1$. In panels (a,b) the peak-to-peak velocity amplitude v_{amp} is plotted as a function of the average headway h^* while in panels (c,d) the flux q is plotted as a functions of the average density $1/h^*$. The right side of panel (a) corresponds to the left side of panel (c) and the same holds for panels (b) and (d). Thick curves correspond to the uniform flow and thin curves correspond to oscillatory (travelling wave) solutions. Stable and unstable states are shown as solid green (light grey) and dashed red (dark grey) curves, respectively. The black dotted curve in panels (c,d) corresponds to the approximation of the flux for $N \to \infty$. Hopf and fold bifurcations are denoted by black stars and blue $\times$-s, respectively. The black dots A-E in panels (b,d) correspond to the time profiles in Fig. 4.

First we fix τ and α and vary h^*, i.e., we study the system along the horizontal line $\alpha=1$ in Figs. 2(c) and 2(d). In Figs. 3(a) and 3(b) the peak-to-peak velocity amplitude

$$v_{\text{amp}} = \max_t v_i(t) - \min_t v_i(t), \tag{16}$$

of the appearing oscillations are shown as a function of the average headway h^*. Note that v_{amp} is the same for every i since the motion of vehicles is identical except a shift in time. We will exploit this property when defining quantities like the flux further below. Solid green (light grey) and dashed red (dark grey) curves correspond to stable and unstable states, respectively. The thick curve along the horizontal axis represents the uniform flow that is stable for small and large values of h^* and unstable for intermediate values. For the oscillatory solutions $v_{\text{amp}} > 0$, as shown by the thin curves. The Hopf bifurcation points—where the uniform flow loses and gains stability—are shown as black stars. The Hopf bifurcations are subcritical, that is, the appearing small amplitude oscillations are unstable. This corresponds to $\delta > 0$ in Eq. (15) that approximates the peak-to-peak amplitude close to the Hopf bifurcation point. The branches of oscillatory solutions fold back for large amplitude resulting in stable oscillations. These fold bifurcation points are marked by blue $\times$-s.

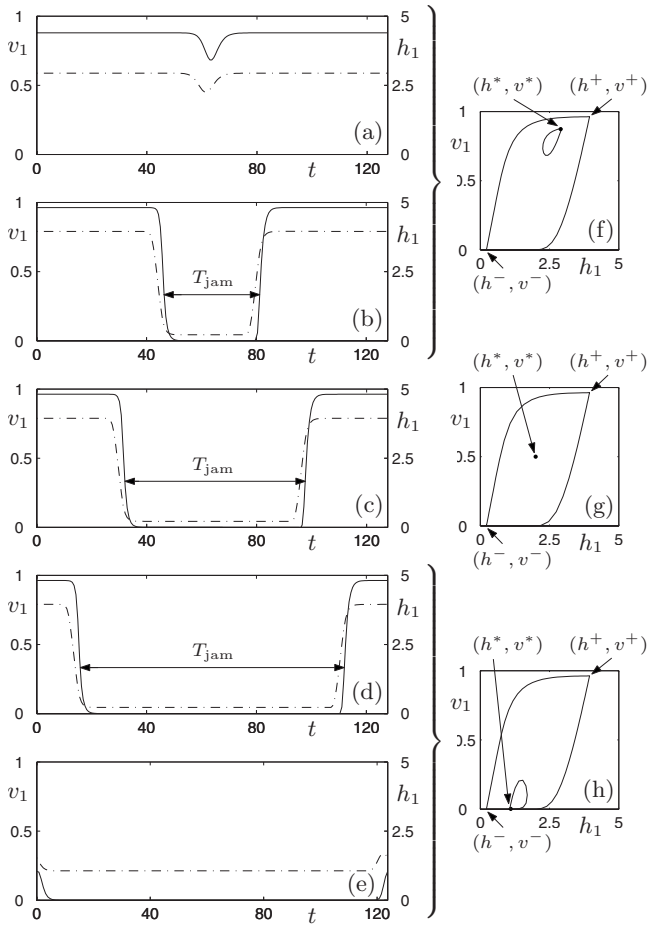

FIG. 4. Oscillations for wave number $k=1$ corresponding to the black dots A-E in Figs. 3(b) and 3(d). In panels (a – e) the velocity of the first vehicle is shown as a solid curve (scaled on the left) while the headway of the first vehicle is shown as a dashed-dotted curve (scaled on the right). Panels (f – h) show the oscillations in state space. Notice that the small-amplitude unstable oscillations (a,e) are similar to homoclinic orbits, while the large-amplitude stable oscillations (b – d) are similar to heteroclinic orbits.

The bifurcation diagrams show that there exist three qualitatively different behaviors:

(i) In the regimes to the left of the left fold point and to the right of the right fold point the only linearly stable state is the uniform flow solution and consequently this state is globally stable.

(ii) In the regime between the two Hopf points the uniform flow is linearly unstable and the only linearly stable state is the large-amplitude oscillatory solution that is consequently globally stable.

(iii) In the regimes between Hopf and fold points both the uniform flow and the large-amplitude oscillatory solutions are linearly stable and they are separated by an unstable oscillatory solution. This means that the system is bistable: depending on the initial conditions either the uniform flow or the oscillatory solution is approached. Observe that the bistable regimes become much more pronounced in the delayed case; the delay makes this behavior very robust. In fact, for certain OV functions [that differ from Eq. (6)] the bistability may disappear for $\tau=0$ but it always exists for large enough τ; see [23].

To reveal the details of the nonlinear dynamics we marked the points A-E along the oscillatory branch in Fig. 3(b). Points A, B are in the bistable regime on the right ($h^*=2.9$), point C is in the regime where the uniform flow is linearly unstable ($h^*=2.0$) and points D,E are in the bistable regime on the left ($h^*=1.1$). Figures 4(a)–4(e) shows the corresponding time profiles for velocity (solid curve) and headway (dashed-dotted curve) for the first vehicle, while panels (f–h) depict the periodic orbits in state space. These solutions preserve the travelling wave features: the time profiles of the other vehicles can be obtained by shifting the oscillations with $T_{\rm p}/N$ where $T_{\rm p}$ is the period of oscillations.

The small-amplitude unstable oscillations in panel (a) consists of a plateau of constant velocity that is interrupted by a "ditch" where the velocity is reduced for a short time (the driver taps the brake shortly). The velocity along the plateau is close to (but slightly higher than) the velocity of the uniform flow Eq. (9). This can be observed in panel (f) where the "corner" of the small-amplitude periodic orbit corresponds to the plateau while the dot at (h^*,v^*) represents the uniform flow. (The ''corner'' and the dot are very close and the dot is located ''inside'' the limit cycle.) The unstable periodic orbit is similar to a homoclinic orbit and for $N \to \infty$ this becomes a homoclinic orbit since the length of the plateau goes to infinity. Moving point A along the unstable oscillatory branch in Fig. 3(b) (from left to right) the velocity is reduced more and more during the ''ditch'' reaching zero at the fold point.

The small-amplitude unstable oscillations in panel (e) are similar to those in panel (a) but here the velocity plateau is interrupted by a "hump" where the velocity is increased for a short period of time. Again, the velocity along the plateau is close to the values of the uniform flow Eq. (9) and the unstable periodic orbit is close to a homoclinic orbit as displayed in panel (h). Moving point E along the unstable oscillatory branch in Fig. 3(b) (from right to left) the velocity increases more and more during the "hump."

The large-amplitude stable oscillations shown in panels (b–d) consist of a high-velocity plateau and a low-velocity plateau that are connected by a ''stop-front'' (where vehicles decelerate) and a "go-front" (where cars accelerate). The corresponding travelling wave is a stop-and-go wave. The oscillations are shown in state space in panels (f–h) where the "corners" of the large-amplitude periodic orbits correspond to the velocity plateaux. The stable periodic orbit is similar to a heteroclinic orbit and for $N \to \infty$ it becomes a heteroclinic orbit since the length of the plateaux become infinite. Observe that the period of oscillations does not change significantly between panels (a–e).

Moving along the stable oscillatory branch in Fig. 3(b) (from right to left) the velocity along the plateaux and the shape of the fronts do not change significantly but the fraction of time spent in the low-velocity state increases. To quantify this change we introduce $T_{\rm jam}$, the time interval corresponding to $v_i(t) < 1/3$. Thus one can define the flux

$$q = \frac{\min_t v_i(t)}{\min_t h_i(t)} \frac{T_{\rm jam}}{T_{\rm p}} + \frac{\max_t v_i(t)}{\max_t h_i(t)} \left(1 - \frac{T_{\rm jam}}{T_{\rm p}}\right), \tag{17}$$

where $T_{\rm p}$ is the period of oscillations. This quantity gives only an approximate value of the flux but it is a good estimate for large N when the width of the plateaux is much smaller than the width of the fronts. Indeed, the choice 1/3 is arbitrary but choosing any other velocity between 0 and 1 only results in small quantitative differences.

In Figs. 3(c) and 3(d) the so-called fundamental diagrams show the flux q as a function of average density $\rho^*=1/h^*$. Note that the right side of panel (a) corresponds to the left side of panel (c) (and vice verse), and the same holds for panels (b) and (d). For the uniform flow one may calculate the flux as

$$q^* = \frac{v^*}{h^*} = \frac{V(h^*)}{h^*} = \rho^* V(\rho^*), \tag{18}$$

that gives the thick concave curve. Considering the spatial wave speed Eq. (14) for $N \gg k$ and $h^*=h^*_{\rm cr}$ one obtains

$$c_0 \approx V(h^*_{\rm cr}) - h^*_{\rm cr} V'(h^*_{\rm cr}) = \left.\frac{dq^*}{d\rho^*}\right|_{\rho^*=1/h^*_{\rm cr}}, \tag{19}$$

which is the derivative of the concave curve at $1/h^*_{\rm cr}$ where the flow loses and gains stability. This is in agreement with the kinetic theory of linear waves [29]. From the fundamental diagram one may notice that c_0 changes sign as one increases the delay, i.e., the unstable small-amplitude waves propagate backward for $\tau=0$ and propagate forward for $\tau=1$. However, this does not persist for large-amplitude waves that always propagate upstream as will be demonstrated in Sec. V B.

Bistability can be observed in the fundamental diagrams and this behavior becomes very robust for the delayed case. Observe that the flux for unstable oscillations is almost the same as the flux of the uniform flow since the velocity changes in a very short time interval in Figs. 3(a) and 3(e). This vindicates that studying only the fundamental diagram is not adequate to reveal the mechanism behind jam formation in the bistable regime but one needs to pay close attention to driver behavior. We remark that to trace the stable part of the fundamental diagram one may use numerical simulations and different vehicle counting methods [30].

A. Large N Limit

Now we compare our results to the large N limit that is taken as $N\to\infty$ while fixing $h^*=L/N$. In particular, we are interested in where the fold points are located for large N. In [22] it was shown that for intermediate values of the headway the system reaches the large N limit fast, that is, no quantitative differences can be found for $N \gtrsim 20$. In this regime we may introduce

$$h^- = \min_t h_i(t), \quad h^+ = \max_t h_i(t),$$

$$v^- = \min_t v_i(t), \quad v^+ = \max_t v_i(t), \tag{20}$$

and realize that

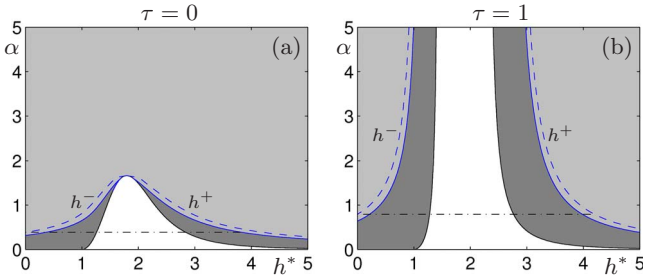

FIG. 5. (Color online) Phase diagrams for wave number $k=1$ comparing the nondelayed and delayed cases. The uniform flow is linearly stable in the light and dark grey domains and unstable in the white domain that is bounded by the solid black Hopf bifurcation curves. Large amplitude oscillations exist in the white and dark grey regimes between the solid blue fold bifurcation curves. Consequently, the system is bistable in the dark grey domains. Dashed blue curves indicate the boundaries of bistability in the $N\to\infty$ limit and collisions occur below the horizontal dashed-dotted lines. Notice that the bistable regimes are much more extended in the case with delay.

$$v^- \approx V(h^-), \quad v^+ \approx V(h^+). \tag{21}$$

These quantities do not change significantly along the stable oscillatory branch except when the parameters are close to the fold bifurcation points.

Furthermore, calculating $T_{\rm jam}$ along the branch we obtain that

$$\frac{T_{\rm jam}}{T_{\rm p}} \approx \frac{h^+ - h^*}{h^+ - h^-}. \tag{22}$$

Substituting Eqs. (20)–(22) into Eq. (17) gives

$$q \approx \frac{V(h^-)}{h^-} \frac{h^+ - h^*}{h^+ - h^-} + \frac{V(h^+)}{h^+} \frac{h^* - h^-}{h^+ - h^-}, \tag{23}$$

that corresponds to the kinetic theory of nonlinear waves [29]. This allows us to calculate the flux along the stable oscillatory branch to any average headway h^* (or average density $1/h^*$) using the quantities h^- and h^+ that are determined from a single (intermediate) value of h^*. Indeed, the larger N is the more accurate are the approximations Eqs. (21)–(23). In Figs. 3(c) and 3(d) the flux Eq. (23) is plotted as a dotted black curve that estimates the solid green (light grey) branch of oscillations with high accuracy (except close to the fold points). The congested state (h^-,v^-) and the free-flow state (h^+,v^+) are shown together with the uniform flow equilibrium (h^*,v^*) in Figs. 4(f)–4(h). In the $N\to\infty$ limit these "quasiequilibria" are connected by heteroclinic orbits.

Formula (22) also reveals what happens at the fold bifurcation points. At the right fold point the length of the low velocity plateau goes to zero ($T_{\rm jam}\approx 0$): almost all vehicles travel with velocity v^+ and they are separated by h^+. That is, the fold bifurcation occurs when $h^*\approx h^+$. Similarly, at the left fold point the length of the high velocity plateau goes to zero ($T_{\rm jam}\approx T_{\rm p}$): almost all vehicles travel with velocity v^- and separated by h^- and so $h^*\approx h^-$. Again, these approximations become more accurate as N is increased.

To check how close the $N=33$ case is to the $N\to\infty$ case, we locate the fold bifurcations and also the limits h^- and h^+ for different values of α. The results are shown in Fig. 5. The solid black curves (separating the white and dark grey regions) are the Hopf bifurcation curves for $k=1$; cf. the outermost curves in Figs. 2(c) and 2(d). The solid blue curves (separating the light and dark grey regions) are the fold bifurcation curves and they are determined by two-parameter numerical continuation. The dashed blue curves show h^- and h^+. These are calculated using Eq. (20) from one-parameter numerical continuation when α is varied and h^* is fixed. The fold curves are very close to the h^- and h^+ curves, which vindicates that the large N limit is well approximated by the $N=33$ case. In the large N limit, one may also determine the boundary of collisions from the h^- curve. Collisions occur for negative h^-, that is, for α values that are below the point where the h^- curve intersects the vertical axis. This boundary is shown Fig. 5 as dashed-dotted horizontal line. Notice that the collision regime is more extended in the delayed case.

Regimes of globally stable uniform flow (outside the fold curves), globally stable stop-and-go oscillations (between the Hopf curves) and bistability (enclosed by Hopf and fold curves) are shaded as light grey, white and dark grey, respectively. Observe that the bistable regime is much larger in the delayed case. For $\tau=0$ it shrinks to zero and disappears as α increases while for $\tau>0$ it persists even for large α, i.e., the delay makes the bistability robust. We emphasize that in the bistable regime the system is excitable: small perturbations decay while large perturbations lead to stop-and-go waves.

B. Bistable Wave Dynamics

In this section we use numerical simulation to investigate the spatiotemporal dynamics induced by bistability. We focus on the regime on the right of Figs. 3(b) and 5(b) and study the excitable dynamics in detail. We demonstrate that one may obtain qualitatively different emergent behaviors by changing only the initial conditions. We also quantify the 'critical' initial conditions that separate different behaviors. Recall that the initial conditions are functions on the interval $t\in[-\tau,0]$ (that are chosen to be constant functions here).

It was shown analytically in [23] that imposing large enough sinusoidal spatial inhomogeneity on the system may lead to stop-and-go waves. However, the time profiles in Fig. 4(a) suggest that even localized perturbations can trigger traffic jams. To test this idea we set the initial conditions as follows: all vehicles are at the uniform flow equilibrium Eq. (9) except one which has its velocity reduced by $v_{\rm per}$ and its headway increased by $h_{\rm per}$. This setup mimics the effect that a driver taps the brake for a short time interval. More precisely, we assume that the selected driver has decelerated with $a_{\rm br}<0$ for the time interval $T_{\rm br}$, and so its velocity is reduced by

$$v_{\rm per}=|a_{\rm br}|T_{\rm br}, \tag{24}$$

and its headway is increased by

$$h_{\rm per}=\tfrac{1}{2}|a_{\rm br}|T_{\rm br}^2. \tag{25}$$

We fix the braking interval $T_{\rm br}$ and vary the braking strength $a_{\rm br}$ to determine the critical perturbation needed to trigger

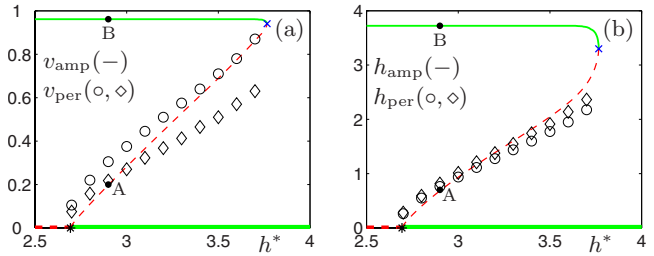

FIG. 6. (Color online) Comparing the peak-to-peak amplitudes Eqs. (16) and (26) of unstable oscillations with the critical strength of localized perturbations Eqs. (24) and (25) for the velocity (a) and the headway (b) in case of $k=1$. The circles ○ and diamonds ◇ correspond to braking intervals $T_{\rm br}=5.0$ and $T_{\rm br}=7.5$.

stop-and-go traffic jams. In Fig. 6(a) the peak-to-peak velocity amplitude Eq. (16) is compared with the critical velocity perturbation $v_{\rm per}$; cf. the right side of the bifurcation diagram in Fig. 3(b). Similarly, in Fig. 6(b) the peak-to-peak headway amplitude

$$h_{\rm amp}=\max_t h_i(t)-\min_t h_i(t), \tag{26}$$

is compared with the critical headway perturbation $h_{\rm per}$. Circles ○ and diamonds ◇ correspond to $T_{\rm br}=5.0$ and $T_{\rm br}=7.5$, respectively. The results vindicate that sufficiently large localized excitations can trigger stop-and-go jams and that the critical excitation increases with the amplitude of unstable oscillations. This demonstrates that a single driver may drive the whole system to the stop-and-go state even though the uniform flow is stable against small perturbations. Indeed, there is no perfect match between the critical excitation and the amplitude since the localized perturbations do not exactly place the system to the unstable manifold of the limit cycle but simply to "one or the other side of the stable manifold" of the limit cycle. Still, the qualitative dynamics of the system is determined by the unstable oscillations.

To illustrate the spatiotemporal dynamics we fix $h^*=2.9$, which corresponds to the dots A,B in Figs. 3(b) and 6 and to the oscillation profiles in Figs. 4(a), 4(b), and 4(f). The results are shown in Fig. 7 where the velocities of every third vehicle are depicted in the top panels (a,b) and the corresponding positions are displayed in the bottom panels (c,d). The initial conditions are chosen according to Eqs. (24) and (25), i.e., we set $\{T_{\rm br}=5.0,\ a_{\rm br}=-0.60\}\Rightarrow\{v_{\rm per}=0.30,\ h_{\rm per}=0.76\}$ on the left panels (a,c) and $\{T_{\rm br}=5.0,\ a_{\rm br}=-0.61\}\Rightarrow\{v_{\rm per}=0.305,\ h_{\rm per}=0.7625\}$ on the right panels (b,d). The latter case corresponds to the circle in Fig. 6 at $h^*=2.9$. The small differences in initial conditions lead to very different emergent behavior. On the left the perturbations decay and the system returns to the uniform flow equilibrium, while on the right perturbations are amplified as they cascade back along the road and a stop-and-go wave develops.

Now we focus on the development of the stop-and-go wave in Figs. 7(b) and 7(d). For $t\lesssim 100$ the small amplitude wave propagates downstream corresponding to $c_0>0$ in Eqs. (14) and (19) but as the amplitude increases a backward propagating stop-and-go wave emerges. We detect when the

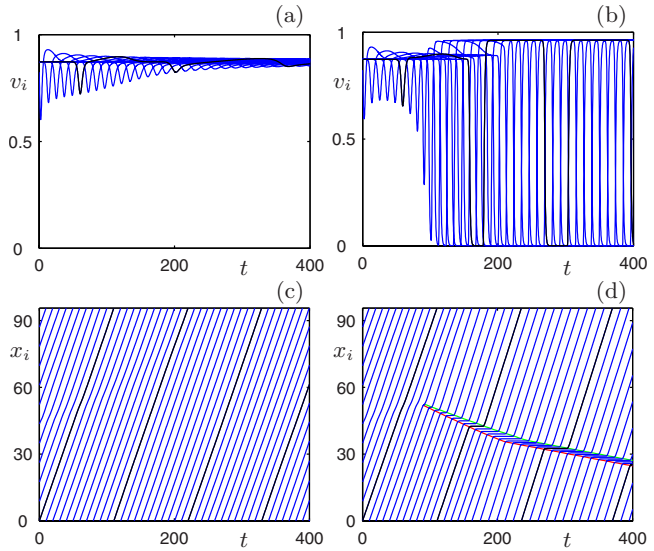

FIG. 7. (Color online) Demonstration of bistability in space-time. In panels (a,b) the velocities of every third vehicle are shown while panels (c,d) display the corresponding positions. The trajectory of the first vehicle is emphasized as black. Observe that the small difference in initial conditions between (a,c) and (b,d) leads to large differences in the emergent state. In panel (d) the stop-front (lower curve) and the go-front (upper curve) are highlighted as red and green, respectively; see Fig. 8(a) for zoom-in. Notice the different spatial wave speed of the developing and the fully developed stop-and-go wave.

velocity of a vehicle drops below 1/3 and this gives the stop-front in space (lower curve, highlighted as red). We also detect when the velocity of a vehicle exceeds 1/3 and this gives the go-front in space (upper curve, highlighted as green). These fronts separate the congested regime (where the velocity is below 1/3) and the free-flow regime in space. Detecting these velocity crossings provides us with discrete points in space time but these are lined up to visualize the front motion. The time evolution of the stop-and-go wave can be described through the motion of the corresponding fronts.

As the wave develops there exist two different stop-and-go regimes with different front behavior and wave

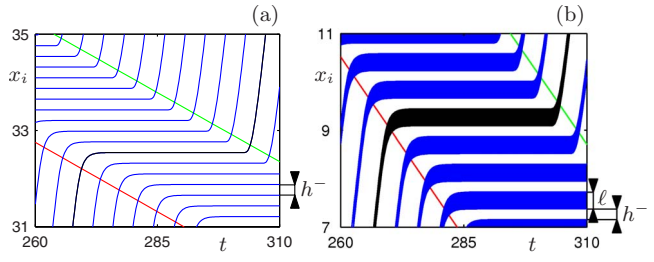

FIG. 8. (Color online) Zoom of Fig. 8(d) is shown in panel (a) when all trajectories are displayed. Panel (b) shows the same situation but with nonzero vehicle length $\ell > 0$. The bottom and the top of a "fat trajectory" correspond to the motion of the front and rear bumper of a vehicle. The stop-front (lower curve) and the go-front (upper curve) are highlighted as red and green, respectively. Observe that the vehicle length alters the wave propagation speed significantly.

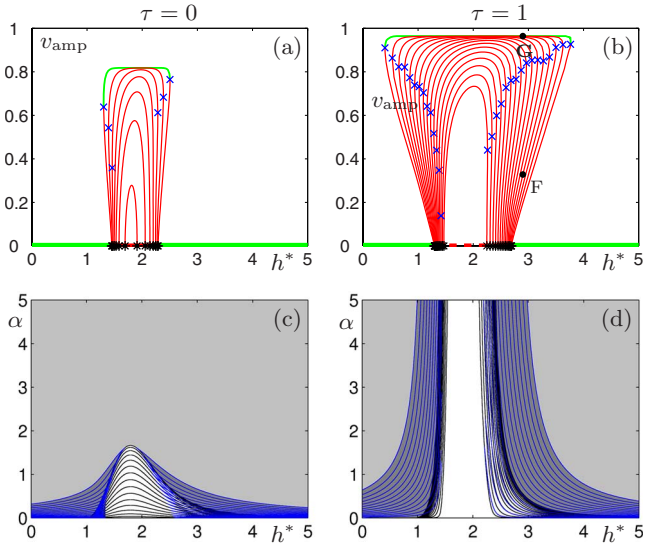

FIG. 9. (Color online) Bifurcation diagrams for $\alpha = 1$ (a,b) and phase diagrams (c,d) comparing the cases without and with reaction time delay for all wave numbers. The same notation is used as in Figs. 3 and 5. In the regimes between the outermost Hopf curve the k-th fold curve (counting from outside to inside) one may excite k stop-and-go waves. The black dots F,G in panel (b) correspond to the time profiles in Fig. 10.

speed. For $100 \lesssim t \lesssim 200$ the stop-front and the go-front propagate upstream with different velocities such that they move away from each other, i.e., the congested region extends. For $t \gtrsim 200$ the fronts propagate with the same velocity and the system reaches the state corresponding to Figs. 4(b) and 4(f). The regime where the velocity is below 1/3 in Fig. 4(b) corresponds to the congested regime in Fig. 7(d). In fact, at a given moment in time most vehicles are either at the congested state (h^-, v^-) or at the free-flow state (h^+, v^+) and only a few cars travel with velocity between v^- and v^+ as shown by the zoom in Fig. 8(a), where the trajectories of all vehicles are displayed.

In the regime $t \gtrsim 200$, the front velocities are well approximated by

$$c = \frac{h^+ v^- - h^- v^+}{h^+ - h^-} < 0, \tag{27}$$

that is obtained from kinetic theory of nonlinear waves [29]. For the parameters considered here we have $c = -0.0567$ that fits very well to Fig. 7(d).

So far we only considered vehicles of zero length, i.e., $\ell = 0$ in Eq. (2). For nonzero ℓ the qualitative dynamics do not change since the dynamical system [Eqs. (3), (4), and (8)] does not contain this parameter. However, the parameter ℓ alters the spatial wave propagation speed of the stop-go-wave significantly according to

$$c_\ell = c\left(1 + \frac{\ell}{h^-}\right). \tag{28}$$

This is demonstrated in Fig. 8(b) where the same spatiotemporal plot is shown as in Fig. 8(a) but for $\ell = 0.35$. This

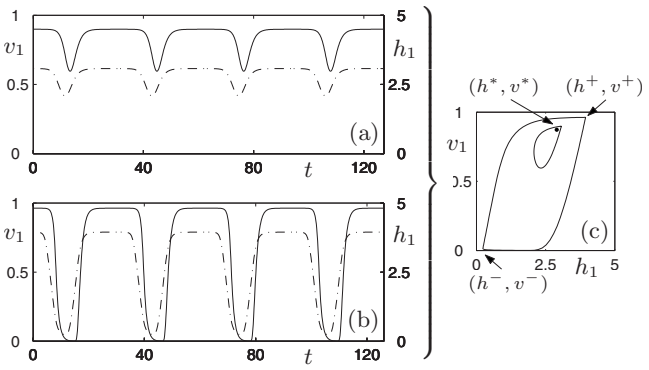

FIG. 10. Oscillations for wave number $k=4$ corresponding to the black dots F,G in Fig. 9(b). Notation and time scales are as in Figs. 4(a), 4(b), and 4(f).

indicates that considering lorries instead of automobiles results in significantly faster wave propagation.

VI. TRIGGERING MULTIPLE JAM FORMATIONS

In this section, we investigate oscillations corresponding to higher wave numbers $k>1$. It was shown in Fig. 2 that such oscillations arise when crossing Hopf bifurcation curves in the linearly unstable parameter domain. The resulting small amplitude oscillations are always unstable but further bifurcations may occur as the amplitude increases.

The velocity amplitude of oscillations are shown in Figs. 9(a) and 9(b) for $\alpha=1$ where the same notation is used as in Figs. 3(a) and 3(b), except that unstable branches are shown as solid red (dark grey) curves. The outermost branch belongs to $k=1$ and k increases from outside to inside. We found that the oscillatory solutions are always unstable for $k>1$. When the Hopf bifurcation is subcritical the oscillatory branch undergoes a fold bifurcation (similarly to the $k=1$ case) but it does not gain stability. In the non-delayed case only the first 7 branches appear. The Hopf bifurcations are subcritical for the outer branches $k=1,\ldots,3$ and supercritical for the inner branches $k=4,\ldots,7$. In the delayed case all 16 branches are present and the Hopf bifurcations are subcritical for all branches. This robust subcriticality leads to extended regions where the stable uniform flow coexist with oscillations belonging to different wave numbers.

Figures 9(c) and 9(d) depict the Hopf and fold curves in the (h^*,α)-plane where the same notation is used as in Figs. 5(a) and 5(b). These figures demonstrate that, similarly to the bistable regions, the regions of coexistence are much more pronounced in the delayed case. The outer fold curves are almost equally spaced: they divide the bistable domain into regions of equal width and the "complexity of the dynamics" (the number of unstable oscillations) increases when moving from outside to inside.

To understand the role of this complexity in the emergent behavior we study the oscillations for $k>1$ in detail. We choose the $k=4$ case to demonstrate the dynamics but the result are qualitatively the same for any $k>1$ with small k/N. We marked the points G,F along the $k=4$ branch in Fig. 9(b) (at $h^*=2.9$) and plot the corresponding oscillations in

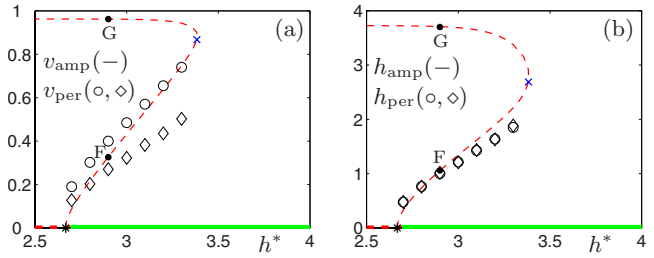

FIG. 11. (Color online) Comparing the peak-to-peak amplitudes Eqs. (16) and (26) of unstable oscillations with the critical strength of localized perturbations Eqs. (24) and (25) for the velocity (a) and the headway (b) in case of wave number $k=4$. The circles ○ and diamonds ◇ correspond to braking intervals $T_{\mathrm{br}}=5.0$ and $T_{\mathrm{br}}=7.5$.

Fig. 10. The same notation and time scales are used as in Figs. 4(a), 4(b), and 4(f), that is, the period of oscillations for $k>1$ is about one k-th of the oscillations for $k=1$. (In general the period is proportional to N/k.) Furthermore, there are remarkable similarities between the $k=1$ and $k>1$ cases considering the shape of the periodic orbits. The velocity of the small-amplitude (homoclinic-like) oscillations plateaus at approximately the same value and only differ in how much the velocity is reduced during the "ditches." For the large amplitude (heteroclinic-like) oscillations the plateaux and the fronts look almost identical. Notice that adding up the time intervals when the velocity is below 1/3 for $k>1$ approximately gives T_{jam} for $k=1$, that is, the time spent in congestion is preserved for small $k>1$.

One may study the stability of these solutions in detail and find that while the small amplitude oscillations are "strongly unstable" (there exist a Floquet multiplier that is much larger than 1 in magnitude), the large amplitude oscillations are only "weakly unstable" (the largest Floquet multiplier is outside the unit circle but very close to it). Due to this weak instability the system can stay in the neighborhood of large amplitude oscillations for long (but still finite) time. This suggest that applying sufficiently large localized perturbations (at k sites) one may excite large amplitude oscillations of wave number k. To observe such excitable behavior the parameters need to be chosen from the regimes between the outermost Hopf curve and the k-th fold curves (counting from outside to inside) in Fig. 9.

Similarly to the $k=1$ case, the critical value of localized perturbations can be determined by numerical simulations for $k>1$. For example, considering $k=4$ we initialize the system into the uniform flow but reduce the velocity and increase the headway of four different vehicles by v_{per} and h_{per} according to Eqs. (24) and (25). Figure 11 compares the peak-to-peak amplitude of oscillations for $k=4$ [cf. the right side of Fig. 9(b)] with the critical perturbations needed to trigger four stop-and-go jams. The results are presented for $T_{\mathrm{br}}=5.0$ (circles ○) and $T_{\mathrm{br}}=7.5$ (diamonds ◇). Observe that the excitable behavior is qualitatively similar to the $k=1$ case; cf. Fig. 6.

To illustrate this excitability in space-time, we fix $h^*=2.9$ that corresponds to the dots F,G in Figs. 9(b) and 11 and to the oscillation profiles in Fig. 10. Using Eqs. (24) and (25) we set the initial conditions as $\{T_{\mathrm{br}}=5.0,\quad a_{\mathrm{br}}=-0.80\}\Rightarrow\{v_{\mathrm{per}}=0.40,\quad h_{\mathrm{per}}=1.0\}$ corre-

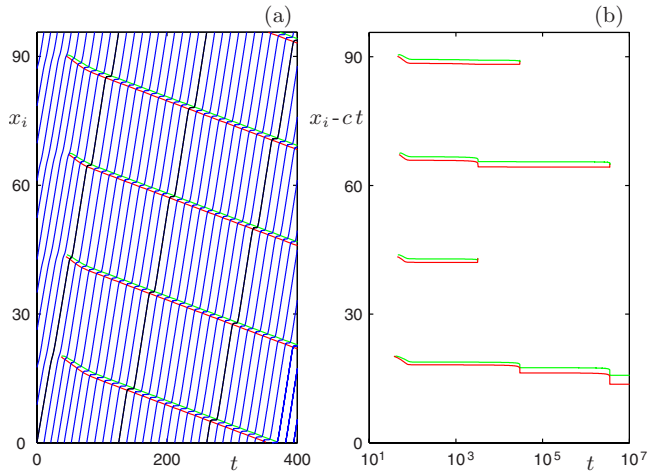

FIG. 12. (Color online) Demonstrating the dynamics of four triggered traffic jams in space-time. In panel (a) the same notation is used as in Fig. 7. In panel (b) the slow dynamics of the arising traffic jams are shown when the constant speed motion is eliminated. A jam disperses when its stop-front (lower red curve) and go-front (upper green curve) meet with each other. Observe that the sum of width of the congested regimes is approximately constant.

sponding to the circle in Fig. 11 at $h^*=2.9$. The spatiotemporal plot in Fig. 12(a) shows the position of every third vehicle and the detected stop-fronts (lower red curves) and go-fronts (upper green curves). These fronts enclose the congested regions where the velocity is below 1/3. Note that the fronts are detected simultaneously as time progresses and it requires further data processing to separate the points for individual fronts.

The fronts travel with almost the same velocity which is well approximated by c in Eq. (27). To reveal the slow dynamics we eliminate this constant velocity motion in Fig. 12(b) and show time on a logarithmic scale. The relative velocity of the fronts with respect to each other is usually very small but there are ''abrupt'' changes when a stop-front and a go-front of a traffic jam approaches each other and the congested regime disperses. Through these dispersions the number of traffic jams gradually decreases to one, that is, the stable stop-and-go wave for $k=1$ is approached. Notice that the sum of the width of congested regimes is approximately constant for any k, i.e., the number of vehicles in congestion is preserved for small $k>1$. We remark that one may trigger k traffic jams using localized perturbations that are not evenly distributed. Still, the slow dynamics of fronts remain qualitatively similar to Fig. 12(b), except that merging of traffic jams may occur as well when the stop-front of a traffic jam approaches the go-front of the neighboring jam. It may be an interesting future research to model the spatiotemporal front dynamics explicitly.

VII. CONCLUSION AND DISCUSSION

In this paper we studied a car-following model with driver reaction time delay. We found that the dynamics of the related DDEs are robustly excitable. Extended regimes are identified in parameter space where the uniform flow is linearly stable but traffic jams can be triggered by large enough localized perturbations. This phenomenon is explained by the existence of unstable small-amplitude oscillations that separate the uniform flow and the large-amplitude stop-and-go solutions. Along the excitable regime the amplitude of critical perturbations decreases as the traffic becomes more and more dense until the regime of spontaneous jam formation is reached. At one end a vehicle must almost stop to trigger a stop-and-go jam: "actions have to be as large as the effects." At the other end there is spontaneous jam formation: "tiny actions have large effects." That is, the delayed car-following model establishes a solid connection between the dynamics of continuum models and the dynamics of non-delayed discrete car-following models.

Our results show that in order to understand the emergent behavior of traffic it is crucial to pay attention to the behavior of individual drivers. A single driver can trigger a stop-and-go wave by tapping the brake hard enough. Doing so, the driver reduces the overall flux of the system significantly. Still if such braking is below a critical limit, the ripples decay and the flow remains smooth. This behavior can only be determined by studying the intricate microscopic dynamics of the system and cannot be concluded by simply looking at flux-density (fundamental) diagrams [31,32].

The obtained dynamics should be taken into account when optimizing ramp metering on highways [33], i.e., when the inflow from on-ramps are controlled by traffic lights based on flow measurements. The current algorithms only consider how much inflow is allowed in order to keep the density on the main highway below a certain limit (that is given by the maximum of the fundamental diagram). Our results vindicate that it is also important that vehicles reach their desired speed before joining the main flow. This may be achieved by long enough on-ramps and letting only one or two vehicles per green period enter the on-ramps.

The diversity of human drivers may still impede our ability to control the emergent behavior of traffic on highways, since it is impossible to eliminate all irregularities of driver behavior (bad lane changes, sudden strong braking). However, many new vehicles are equipped with Autonomous Cruise Control devices that are able to measure distances between vehicles and actuate the cars accordingly. Time delays arise in these system due to the time required for sensing, computation and actuation. These are smaller than the human reaction time but still need to be considered when designing the control algorithms [34,35]. Furthermore, the effects of uncertainties may also need to be considered in these decentralized control systems [36].

ACKNOWLEDGMENTS

One of the authors (G.O.) acknowledges discussions with Jeff Moehlis and Francesco Bullo. This research was supported by the Institute for Collaborative Biotechnologies under Grant No. DAAD19-03-D004 from the U.S. Army Research Office, by the Hungarian National Science Foundation under Grant No. OTKA K68910, and by the EPSRC under Grant No. EP/E055567/1.

[1] D. Helbing, Rev. Mod. Phys. **73**, 1067 (2001).
[2] C. F. Daganzo, M. J. Cassidy, and R. L. Bertini, Transp. Res., Part A: Policy Pract. **33**, 365 (1999).
[3] A. Aw and M. Rascle, SIAM J. Appl. Math. **60**, 916 (2000).
[4] M. Bando, K. Hasebe, A. Nakayama, A. Shibata, and Y. Sugiyama, Phys. Rev. E **51**, 1035 (1995).
[5] M. Treiber, A. Hennecke, and D. Helbing, Phys. Rev. E **62**, 1805 (2000).
[6] M. Bando, K. Hasebe, K. Nakanishi, and A. Nakayama, Phys. Rev. E **58**, 5429 (1998).
[7] E. N. Holland, Transp. Res., Part B: Methodol. **32**, 141 (1998).
[8] M. Treiber, A. Kesting, and D. Helbing, Physica A **360**, 71 (2006).
[9] I. Gasser, G. Sirito, and B. Werner, Physica D **197**, 222 (2004).
[10] Y. Igarashi, K. Itoh, K. Nakanishi, K. Ogura, and K. Yokokawa, Phys. Rev. E **64**, 047102 (2001).
[11] H. Y. Lee, H.-W. Lee, and D. Kim, Phys. Rev. Lett. **81**, 1130 (1998).
[12] L. A. Safonov, E. Tomer, V. V. Strygin, Y. Ashkenazy, and S. Havlin, Chaos **12**, 1006 (2002).
[13] R. E. Wilson, Philos. Trans. R. Soc. London, Ser. A **366**, 2017 (2008).
[14] D. Helbing and M. Moussaid, Eur. Phys. J. B **69**, 571 (2009).
[15] M. R. Flynn, A. R. Kasimov, J.-C. Nave, R. R. Rosales, and B. Seibold, Phys. Rev. E **79**, 056113 (2009).
[16] F. Siebel and W. Mauser, SIAM J. Appl. Math. **66**, 1150 (2006).
[17] S. A. Campbell, in *Handbook of Brain Connectivity*, edited by V. K. Jirsa and A. R. McIntosh (Springer, New York, 2007), pp. 65–90.
[18] B. Ermentrout and T.-W. Ko, Philos. Trans. R. Soc. London, Ser. A **367**, 1097 (2009).
[19] B. Novák and J. J. Tyson, Nat. Rev. Mol. Cell Biol. **9**, 981 (2008).
[20] P. Berg and R. E. Wilson, in *Traffic and Granular Flow '03*, edited by S. P. Hoogendoorn, S. Luding, P. H. L. Bovy, M. Schreckenberg, and D. E. Wolf (Springer, New York, 2005).
[21] G. Orosz, R. E. Wilson, and B. Krauskopf, Phys. Rev. E **70**, 026207 (2004).
[22] G. Orosz, B. Krauskopf, and R. E. Wilson, Physica D **211**, 277 (2005).
[23] G. Orosz and G. Stépán, Proc. R. Soc. Lond. A **462**, 2643 (2006).
[24] D. Roose and R. Szalai, in *Numerical Continuation Methods for Dynamical Systems*, edited by B. Krauskopf, H. M. Osinga, and J. Galan-Vioque (Springer, New York, 2007), pp. 359–399.
[25] R. Sipahi and S.-I. Niculescu, in *2008 American Control Conference*, (AACC, Seattle, WA), pp. 4922–4927.
[26] E. J. Doedel, A. R. Champneys, T. F. Fairgrieve, Y. A. Kuznetsov, B. Sandstede, and X. Wang, Department of Computer Science, Concordia University, 1997 (unpublished); htp://cmvl.cs.concordia.ca/auto/.
[27] K. Engelborghs, T. Luzyanina, and G. Samaey, Department of Computer Science, Katholieke Universiteit Leuven, Tech. Rep. No. TW-330, 2001 (unpublished); htp://twr.cs.kuleuven.be/research/software/delay/ddebiftool.shtml.
[28] R. Szalai, Department of Engineering Mathematics, University of Bristol, 2008 (unpublished); htp://seis.bris.ac.uk/~rs1909/pdde/.
[29] M. J. Lighthill and G. B. Whitham, Proc. R. Soc. Lond. A **229**, 317 (1955).
[30] T. Seidel, I. Gasser, and B. Werner, SIAM J. Appl. Dyn. Syst. **8**, 1305 (2009).
[31] B. S. Kerner, Phys. Rev. Lett. **81**, 3797 (1998).
[32] M. Schönhof and D. Helbing, Transp. Res., Part B: Methodol. **43**, 784 (2009).
[33] G. Gomes, R. Horowitz, A. A. Kurzhanskiy, P. Varaiya, and J. Kwon, Transp. Res., Part C: Emerg. Technol. **16**, 485 (2008).
[34] A. Kesting and M. Treiber, Comput. Aided Civ. Infrastruct. Eng. **23**, 125 (2008).
[35] A. Kesting, M. Treiber, M. Schönhof, and D. Helbing, Transp. Res., Part C: Emerg. Technol. **16**, 668 (2008).
[36] B. Bamieh, M. R. Jovanovic, P. Mitra, and S. Patterson, (unpublished).